A Nontectonic Origin for the Present-Day Stress Field in the Paris Basin (France)

V. Magnenet, F.H. Cornet, C. Fond

AGU PUBLICATIONS

JGR

Journal of Geophysical Research: Solid Earth

RESEARCH ARTICLE
10.1002/2017JB014345

Special Section:
Rock Physics of the Upper Crust

A Nontectonic Origin for the Present-Day Stress Field in the Paris Basin (France)

V. Magnenet[1], F. H. Cornet[2], and C. Fond[1]

[1]ICUBE, Illkirch-Graffenstaden, France, [2]IPGS, Strasbourg, France

Key Points:
- No present-day deformation has been detected in the French Paris Basin, yet significant deviatoric stresses are measured in limestone formations
- The stress field is not related to tectonics but only to gravity acting on the series of viscoelastic orthotropic geomaterials that fill up the basin
- Stress measurements or observation of present-day deformations in sediments cannot be directly transposed to greater depths

Correspondence to:
V. Magnenet,
vmagnenet@unistra.fr

Citation:
Magnenet, V., Cornet, F. H., & Fond, C. (2017). A nontectonic origin for the present-day stress field in the Paris Basin (France). *Journal of Geophysical Research: Solid Earth*, *122*, 9313–9327. https://doi.org/10.1002/2017JB014345

Received 18 APR 2017
Accepted 19 SEP 2017
Accepted article online 23 SEP 2017
Published online 11 NOV 2017

The copyright line for this article was changed on 20 NOV 2017 after original online publication.

Abstract The large-scale stress patterns observed in intraplate areas are often considered to result from far-field boundary forces that drive plate tectonics. However, no present-day deformation has been detected in the French Paris Basin, yet significant deviatoric stresses are measured in limestone formations observed above soft argillite layers encountered in this region. Further, the pore pressure measured in the argillite is larger than that measured in the surrounding permeable zones. These observations suggest a presently active source of stress in this sedimentary system. We propose that this stress field is not related to tectonics but only to gravity acting on the series of viscoelastic orthotropic geomaterials that fill up the basin. This viscoelastic response is linked to pressure solution effects activated by pore pressure transients related to climatic variations. These pressure transients develop in the fracture system that affects some of the geomaterials and imply a time-dependant deformation field, with time constants related to those of climatic variations. This model outlines the influence of time-dependent material properties on the present-day stress and pore pressure fields that prevail at various depths. It may be considered as a possible loading mechanism for the analysis of intraplate seismicity.

1. Introduction

Extensive stress measurements have been conducted in the upper sedimentary formations of the eastern Paris Basin (France), for the Underground Research Laboratory on nuclear waste storage, near the small village of Bure, Meuse (Cornet & Roeckel, 2012; Wileveau et al., 2007). Their depth range extends from the base of the Dogger limestones (about 750 m below ground level) up to the top of the Oxfordian limestones (about 350 m below ground). Results outline a significant difference between the maximum and the minimum principal stress magnitudes in both the Dogger and the Oxfordian limestone formations. But the difference between the magnitudes of the two horizontal principal stress components measured in the Callovo-Oxfordian argillite layer, in between the two limestone layers, is much smaller (Figure 1). In addition, Delay et al. (2007) have described an overpressure in the argillite that exhibits a parabolic vertical profile, which remains yet unexplained. Classical sources of overpressure in sedimentary basins are compaction, fluid migration, diagenesis, tectonic stress, or more simply topography (e.g., de Marsily, 1986; Neuzil, 1995; Schmalholz et al., 2014). These various effects together with osmotic effects have been investigated (Gonçalves, Violette, Guillocheau et al., 2004; Gonçalves, Violette & Wendling, 2004). They were shown not to be able to explain the complete measured profile.

The Oxfordian limestones exhibit a very small dip and outcrops some tens of kilometers east of the site where stress measurements have been conducted. Further, the Paris Basin is known to be free of significant present-day active tectonics, as evidenced by the absence of microseismic activity (Cara et al., 2015) and by the absence of detectable horizontal strain rate according to repeated GPS measurements (Nocquet, 2012). Hence, a question arises concerning the origin of both the deviatoric stresses in the various sedimentary layers and the parabolic pore pressure profile in the argillite.

Various attempts have been made at modeling this stress field. Assuming an elastic response of the rock mass, Gunzburger and Cornet (2007) have discussed the effect of erosion and that of a far-field uniform horizontal velocity on the local stress field. They conclude that such a combination of loading mechanisms should result in equal vertical gradients for both horizontal principal stress components within a given sedimentary layer, a conclusion not supported by measurements. In addition, Gunzburger and Cornet (2007) do not address the pore pressure parabolic vertical profile in the argillite.

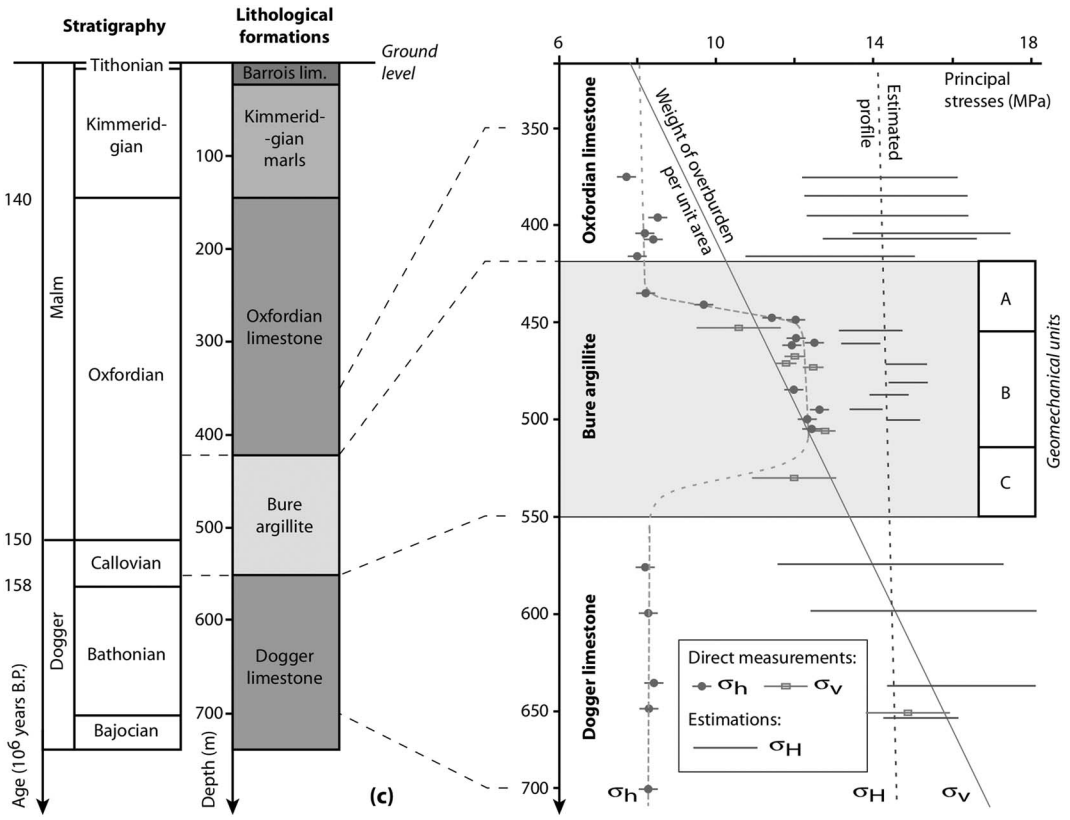

Figure 1. Vertical stress profiles measured at Bure, in the eastern Paris sedimentary basin (Gunzburger & Cornet, 2007).

Gunzburger and Magnenet (2014) have also undertaken an investigation of the elastic material properties that are required for producing the vertical stress profiles reported by Wileveau et al. (2007). They assume linear vertical variations for both horizontal principal stress components applied to the vertical boundaries of their model. The principal stress directions are supposedly related to the Alpine "push" that occurred late Miocene, from 8 to 6 Ma ago. We refer to this elastic model as the "G-M elastic model." Despite an apparent good fit between observations and model predictions, the G-M elastic model suffers some limitations and inconsistencies with observations that are enumerated hereafter.

1. The G-M elastic model assumes an elastic behavior for the argillite, a feature not consistent with results from experimental investigations. Indeed, laboratory measurements have suggested that the argillite cannot sustain a static differential stress over more than a thousand years so that stress conditions that prevailed at the end of the Alpine phase cannot coincide with those observed today.
2. Also, shear wave splitting observations (Lefeuvre et al., 1992) imply some anisotropy for the elastic parameters of some of the layers above the Callovo-Oxfordian argillite.
3. Finally, the hypothesis of an elastic response of the whole system to a late Miocene straining cannot explain the overpressure profile measured presently in the pore fluids of the Callovo-Oxfordian argillite, as discussed by Gonçalves, Violette, and Wendling (2004). Indeed, by now, pore pressure variations linked to tectonic loading should have completely dissipated.

Recently, Calais et al. (2016) have noted that the seismicity observed in stable continental regions (earthquakes) is not consistent with loading rates applied at plate boundaries. They consider that these earthquakes are better explained by a release of elastic energy associated with local transient perturbations.

In the present paper we argue that the development of pressure solution in fractures constitutes a presently active loading source for the sedimentary formations of the Paris Basin. In the final discussion, we observe that such a fluid-solid chemical interaction may be part of the new paradigm proposed by Calais et al. (2016) for explaining intraplate seismicity.

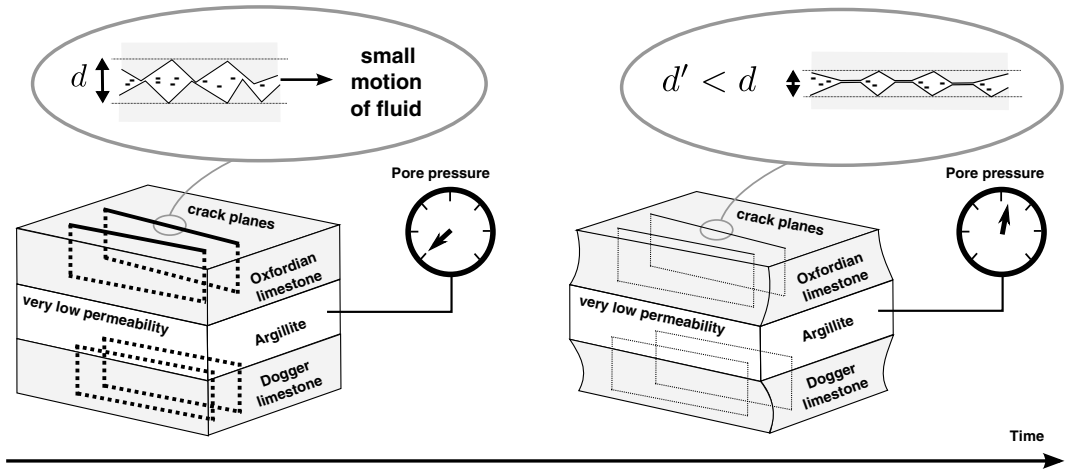

Figure 2. Schematic representation of pressure-solution effects in fractures. As time passes, the tip of asperities gets dissolved and the apparent "thickness" of the fracture decreases.

2. Pressure Solution as a Loading Mechanism

In their attempt at modeling the vertical stress profiles observed at Bure, Gunzburger and Cornet (2007) noticed that best fitting elastic parameters identified for the limestones were much lower than values computed from elastic waves propagation data derived from sonic logs. They were led to conclude on the existence of a long-term softening process affecting the limestone behavior, which they proposed to link to pressure solution effects. In this paper, we follow this conclusion and propose a simple phenomenological hydromechanical model characterized by two main features linked to pressure solution effects: (i) a time-dependent orthotropic mechanical behavior associated with pressure solution in fractures and (ii) a coupling term in the fluid mass balance equation involving volumetric strain. We show that such a one-dimensional vertical viscoelastic model supplemented by some calculations in the horizontal directions is consistent with both the observed stress and pore pressure vertical profiles.

Before pursuing, let us recall that pressure solution is a solid-fluid interaction process that takes place in fluid-saturated materials in the immediate vicinity of zones of high stress concentration where ions migrate from the solid phase to the liquid phase. Hence, pressure solution modifies both the grain size and the porosity of rocks. This mechanism of stress enhanced dissolution has been quite extensively investigated for the last 30 years (Gratier & Guiguet, 1986; Gundersen et al., 2002; Schneider et al., 1996). In particular, it is generally accepted that pressure solution occurs only when stress magnitudes are above a certain threshold value that depends on temperature among other parameters. This physicochemical, nanoscale, mechanism, which depends strongly on environmental conditions, may be modeled by a solid-type, viscoelastic behavior with viscosities that range from 10^{19} Pa s to 10^{25} Pa s (Gratier, 1993; Holl & Anastasio, 1995; Laubsher, 1975; Talbot, 1999).

As pointed out by Yasuhara and Elsworth (2004), a natural fracture is a privileged site for the development of pressure solution. Indeed, fracture surfaces exhibit asperities at all scales, which leads to a large distribution of zones with various stress concentrations. This generates microdisplacements in the direction normal to the fracture plane (see Figure 2). Hence, for a large volume of rock, the cumulated effect of pressure solution in the fracture network is associated with a volume decrease, the geometry of which depends on the fracture network morphology. At Bure, where the detailed stress measurements have been conducted, it is well established that there is virtually no fracture in the argillite layer but that numerous fractures are present in the surrounding limestone layers (André et al., 2006). Interestingly, a statistical analysis of the orientations of all fractures observed in the limestones that underlay and overlay the argillite formation has outlined the existence of a very clear preferential fracture orientation (N 150°E), that is, a direction parallel to the maximum horizontal principal stress direction (Figure 3). Lefeuvre et al. (1992) have discussed results from vertical seismic profiles in some deep (1,860 m) boreholes located some hundred kilometers west from the location where stress measurements have been conducted. They identify some shear wave splitting, which is characteristic of wave propagation in anisotropic materials. Such an anisotropic behavior is detected for both limestone

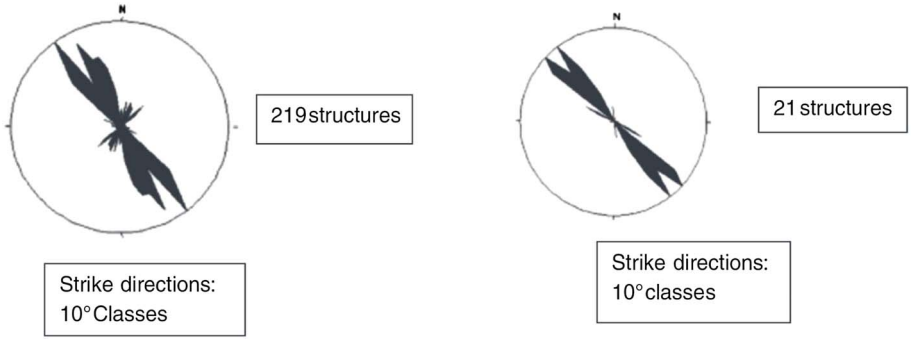

Figure 3. Results from statistical analysis of fractures orientations in the Dogger and Oxfordian limestones. See Cornet and Roeckel (2012, and the references therein).

formations underlying and overlying the Callovo-Oxfordian argillite. The fastest shear wave direction occurs in a direction parallel to that of the maximum horizontal principal stress direction. So these observations support the hypothesis that these limestones exhibit an orthotropic behavior controlled by the fracture pattern and by the sedimentary structure. These anisotropic properties may be linked to the Alpine push of the past.

In addition to these various issues, the relevancy of considering an orthotropic behavior for geological layers at the Bure laboratory is supported by the fact that it does reproduce the observed stress profiles. To illustrate this idea, let us consider an elastic orthotropic geomaterial so that two of its axes of symmetry are horizontal. We call h and H these two horizontal directions. Let v be the vertical direction so that H, h, and v define an orthonormal frame of reference, ($\boldsymbol{e}_H$, $\boldsymbol{e}_h$, and $\boldsymbol{e}_v$). We assume hereafter that these directions are also those of the principal stress directions existing in the body under consideration, with σ_H and σ_h, respectively, the maximum and minimum horizontal principal stress components. A material with orthotropic elastic properties implies nine independent constants of elasticity, which we call E_{HH}, E_{hh}, E_{vv}, ν_{Hv}, ν_{Hh}, ν_{hv}, G_{hv}, G_{hH}, and G_{Hv} by analogy with the significance of the Young's modulus E, the Poisson's ratio ν, and the shear modulus G of isotropic materials. Linear elasticity implies that strain $\boldsymbol{\epsilon}$ is proportional to stress $\boldsymbol{\sigma}$ (both being here written as six components vectors), so that $\boldsymbol{\epsilon} = \mathbb{S} \cdot \boldsymbol{\sigma}$, where $\mathbb{S}$ is the compliance tensor (rewritten hereafter as a matrix):

$$\mathbb{S} = \begin{bmatrix} \frac{1}{E_{HH}} & -\frac{\nu_{Hh}}{E_{HH}} & -\frac{\nu_{Hv}}{E_{HH}} & 0 & 0 & 0 \\ -\frac{\nu_{Hh}}{E_{HH}} & \frac{1}{E_{hh}} & -\frac{\nu_{hv}}{E_{hh}} & 0 & 0 & 0 \\ -\frac{\nu_{Hv}}{E_{HH}} & -\frac{\nu_{hv}}{E_{hh}} & \frac{1}{E_{vv}} & 0 & 0 & 0 \\ 0 & 0 & 0 & \frac{1}{2G_{hv}} & 0 & 0 \\ 0 & 0 & 0 & 0 & \frac{1}{2G_{Hv}} & 0 \\ 0 & 0 & 0 & 0 & 0 & \frac{1}{2G_{Hh}} \end{bmatrix}. \tag{1}$$

Observe that for orthotropic materials, $\nu_{Hv} \neq \nu_{vH}$, and that $(\nu_{Hv}/E_{HH}) = (\nu_{vH}/E_{vv})$, with similar relationships for the other directions. Let us consider a semi-infinite space filled up with such a material and loaded under gravity only. For these loading conditions there is no displacement in any horizontal direction (oedometric loading conditions). In that case, the horizontal principal stress components are linear functions of depth z:

$$\sigma_H = K_H \gamma z, \quad \sigma_h = K_h \gamma z \tag{2}$$

with γ the specific weight and

$$K_H = \frac{\nu_{Hh}\nu_{hv} + \nu_{Hv}}{1 - \nu_{Hh}^2/\chi_{Hh}}, \quad K_h = \frac{\nu_{hv} + \nu_{Hh}\nu_{Hv}/\chi_{Hh}}{1 - \nu_{Hh}^2/\chi_{Hh}}, \tag{3}$$

where $\chi_{Hh} = E_{HH}/E_{hh}$. It may be verified that for an isotropic material we obtain the classical result

$$K_H = K_h = \frac{\nu}{1-\nu}. \tag{4}$$

With such an anisotropic model, it is possible to generate with gravity loading only a regional stress field with vertical and horizontal principal stress directions and different values for the minimum and the maximum horizontal principal stress magnitudes. In this example, the K_h and K_H parameters depend directly

on the geomaterials elastic parameters. Thus, the existence of different values for the horizontal principal stress magnitudes does not necessarily imply a tectonic activity. It may result simply from the anisotropy of the elastic properties for some of the geomaterials of concern.

At this stage, we have outlined that pressure solution in fractures is an active loading mechanism that may be a good candidate to explain observed stress profiles. We argue now that pressure solution occurs at a rate slow enough that no measurable strain may be detected but yet with pore volume variations large enough for generating a significant part of the overpressure observed in argillite. To validate this hypothesis, we propose a hydromechanical viscoelastic model that reproduces the measured horizontal stress as well as the observed pore pressure profiles.

In order to introduce a mathematical description of pressure solutions effects, we modify first the fluid mass balance by introducing an additional term that accounts for the volumetric strain due to dissolution of some solid into the fluid and its precipitation somewhere else. Second, we introduce time dependent elastic properties for the various geological materials. The entire set of governing equations, as well as the numerical method used for their solution, are presented in the next section.

3. A Coupled Poroelastic Model

3.1. Governing Equations

The governing equations are those of linear poroelasticity as developed by Coussy (2004). We assume that limestones and argillite in the vicinity of the Bure laboratory can be idealized as homogeneous, fully saturated, poroelastic materials. We consider only small perturbations and assume local equilibrium conditions, while the only specific force is gravity. In our notation system, tensorial quantities are boldfaced, and any quantity associated with the saturating fluid is subscripted by "$_f$."

If we admit that pressure solution involves dissolution and precipitation processes, the mass variation of an elementary representative volume of porous medium $\mathrm{d}\Omega$ can be split into three contributions: the mass variation of solid grains $\mathrm{d}M_s - \mathrm{d}M_s^0 = m_s \mathrm{d}\Omega$, the mass variation of pure fluid $\mathrm{d}M_f^{\mathrm{pure}} - \mathrm{d}M_f^{\mathrm{pure},0} = m_f^{\mathrm{pure}} \mathrm{d}\Omega$, and the mass variation of solid in solute form $\mathrm{d}M_{\mathrm{sol}} - \mathrm{d}M_{\mathrm{sol}}^0 = m_{\mathrm{sol}} \mathrm{d}\Omega$, where all quantities $m_\bullet$ (kg m^{-3}) denote mass variations per unit of volume of porous medium. According to Coussy (2004), the mass balance inside $\mathrm{d}\Omega$ can be written as

$$\frac{\partial m_s}{\partial t} = -\beta_{s\to\mathrm{sol}} + \beta_{\mathrm{sol}\to s}, \tag{5}$$

$$\frac{\partial m_{\mathrm{sol}}}{\partial t} + \nabla . \boldsymbol{M}_{\mathrm{sol}} = \beta_{s\to\mathrm{sol}} - \beta_{\mathrm{sol}\to s}, \tag{6}$$

$$\frac{\partial m_f^{\mathrm{pure}}}{\partial t} + \nabla . \boldsymbol{M}_f^{\mathrm{pure}} = 0, \tag{7}$$

in which $\boldsymbol{M}_X$ (kg m^{-2} s^{-1}) denotes the vectorial flow of X, that is, the mass of X entering $\mathrm{d}\Omega$ via its boundary $\partial(\mathrm{d}\Omega)$ per unit of time. The source terms $\beta_{s\to\mathrm{sol}}$ and $\beta_{\mathrm{sol}\to s}$ reveal the variation of solid and solute mass due to dissolution and precipitation, respectively. If we introduce the mass content $m_f = m_f^{\mathrm{pure}} + m_{\mathrm{sol}}$ of "real" fluid—that is, the pure fluid plus the solute it transports—as well as its associated vectorial flow $\boldsymbol{M}_f = \boldsymbol{M}_{\mathrm{sol}} + \boldsymbol{M}_f^{\mathrm{pure}}$, then adding equations (6) and (7) leads to

$$\frac{\partial m_f}{\partial t} + \nabla . \boldsymbol{M}_f = \beta_{s\to\mathrm{sol}} - \beta_{\mathrm{sol}\to s} = \beta. \tag{8}$$

In this first approach, we assume that the vectorial fluid flow $\boldsymbol{M}_f$ satisfies Darcy law with a constant, uniform fluid density ρ_f (kg m^{-3}):

$$\boldsymbol{M}_f = \frac{\rho_f K^{\mathrm{int}}}{\mu_f} \left(-\boldsymbol{\nabla} p_f + \rho_f \boldsymbol{g} \right), \tag{9}$$

where μ_f (Pa s) is the fluid dynamic viscosity, K^{int} (m^2) is the intrinsic permeability, and p_f is the fluid pressure. For a saturated medium, m_f is given by

$$m_f = \rho_f \phi (1 + \epsilon_v) - \rho_f \phi_0, \tag{10}$$

where ϵ_v is the volumetric strain, ϕ is the Eulerian porosity, and ϕ_0 is its initial value. The porosity variation is described by the equation

$$\mathrm{d}\phi = (b - \phi)\left(\mathrm{d}\epsilon_v + \frac{\mathrm{d}p_f}{K_s}\right) \tag{11}$$

in which b (1) and K_s (N m^{-2}) correspond, respectively, to the Biot coefficient and to the bulk modulus of solid grains.

The mechanical equilibrium can be written as

$$\boldsymbol{\nabla}.\boldsymbol{\sigma} + r\boldsymbol{g} = \mathbf{0}, \tag{12}$$

where $\boldsymbol{\sigma}$ (N m^{-2}) is the total stress tensor, r (kg m^{-3}) is the homogenized density and $\boldsymbol{g}$ (N kg^{-1}) is the gravity. The density is split into two terms:

$$r = r_0 + m_f \tag{13}$$

in which r_0 (kg m^{-3}) is the initial homogenized density. All material properties—except the mechanical properties discussed later—are considered to be constant and homogeneous in each geological unit.

A common practice, when investigating the hydromechanical behavior of a porous medium, is to split the total stress into an effective stress $\boldsymbol{\sigma}'$ (N m^{-2}) and a hydraulic stress $\boldsymbol{\sigma}_f$ (N m^{-2}), so that $\boldsymbol{\sigma} = \boldsymbol{\sigma}' + \boldsymbol{\sigma}_f$. We add an additional term $\boldsymbol{\sigma}^{\mathrm{inst}}$ (N m^{-2}) for introducing the evolution with time of the elastic properties (see below and section 3.2). The stress decomposition becomes

$$\boldsymbol{\sigma} = \boldsymbol{\sigma}' + \boldsymbol{\sigma}_f + \boldsymbol{\sigma}^{\mathrm{inst}} = \boldsymbol{\sigma}' - b\pi_f + \boldsymbol{\sigma}^{\mathrm{inst}}. \tag{14}$$

In this last equation $\pi_f = p_f - p_f^0$ is the relative fluid pressure, that is, the actual fluid pressure compared to its initial value. The mechanical behavior of the equivalent solid continuum is assumed to be elastic and linear, but with properties varying with time:

$$\partial_t \boldsymbol{\sigma}' = \mathbb{C}(t) : \partial_t \boldsymbol{\epsilon} \tag{15}$$

(without explicit notations, the elastic stiffness $\mathbb{C}(t)$ is assumed to correspond to drained conditions). From (14) and (15), the total stress may be written finally as

$$\boldsymbol{\sigma}(t) = \left[\int_0^t \mathbb{C}(\tau) : \partial_\tau \boldsymbol{\epsilon}\, \mathrm{d}\tau\right] - b\pi_f + \boldsymbol{\sigma}^{\mathrm{inst}}. \tag{16}$$

3.2. Application to the Bure Site

The strain $\boldsymbol{\epsilon}$ and the stress $\boldsymbol{\sigma}$ are described by their respective matrices. We return now to the orthonormal frame of reference ($\boldsymbol{e}_H$, $\boldsymbol{e}_h$, and $\boldsymbol{e}_v$) aligned with the principal stress directions and we assume oedometric boundary conditions:

$$\boldsymbol{\epsilon} = \begin{pmatrix} 0 & 0 & 0 \\ 0 & 0 & 0 \\ 0 & 0 & \epsilon_v \end{pmatrix}_{(\boldsymbol{e}_H, \boldsymbol{e}_h, \boldsymbol{e}_v)}. \tag{17}$$

The space variables associated with ($\boldsymbol{e}_H$, $\boldsymbol{e}_h$, and $\boldsymbol{e}_v$) are denoted x, y, and z, respectively. We focus now on the three geological layers encountered at the Bure underground laboratory and in which stress measurements have been carried out: (1) Oxfordian limestone for $z \in [-445; 0]$ m (445 m in thickness); (2) argillite for $z \in [-556; -445]$ m (111 m in thickness); and (3) Dogger limestone for $z \in [-783; -556]$ m (227 m in thickness), and we assume that these layers are the site of pressure solution effects that depend on the local material properties. Mathematically, we recall that these effects are integrated in our model by two contributions: (1) a source term in the mass balance (β) due to dissolution/precipitation and generating a volumetric strain even at the drained state ($\pi_f = 0$) and (2) a "slow" transition between isotropic elastic properties $\mathbb{C}^{\mathrm{iso}}$ toward drained orthotropic properties $\mathbb{C}^{\mathrm{ort}}$.

This evolution reveals the preferential effect of pressure solution in the direction orthogonal to that of the fractures (direction of σ_h). More precisely, we postulate the following time dependence:

$$\mathbb{C}(t) = \mathbb{C}^{\mathrm{iso}} + \frac{t}{\tau_{\mathrm{ps}}}\left(\mathbb{C}^{\mathrm{ort}} - \mathbb{C}^{\mathrm{iso}}\right), \quad t \in [0; \tau_{\mathrm{ps}}], \tag{18}$$

where parameter τ_{ps} (s) is a time constant associated with pressure solution effects on the materials orthotropy. Note that $\mathbb{C}(0) = \mathbb{C}^{iso}$ and that $\mathbb{C}(\tau_{ps}) = \mathbb{C}^{ort}$ and that a linear transition between $\mathbb{C}^{iso}$ and $\mathbb{C}^{ort}$ is considered in the time interval $[0; \tau_{ps}]$. If we focus on orthotropic materials, the whole stress field is governed by the sole components C_{Hv}, C_{hv}, and C_{vv} of the stiffness tensor $\mathbb{C}$. In that case, a more convenient parameterization can be introduced by defining α_H and α_h as follows:

$$\alpha_H = \frac{C_{Hv}^{ort} - C_{Hv}^{iso}}{C_{Hv}^{iso}} \text{ and } \alpha_h = \frac{C_{hv}^{ort} - C_{hv}^{iso}}{C_{hv}^{iso}}. \tag{19}$$

Indeed, equation (18) leads to

$$C_{Hv}(t) = C_{Hv}^{iso}\left(1 + \alpha_H \frac{t}{\tau_{ps}}\right), \tag{20}$$

$$C_{hv}(t) = C_{hv}^{iso}\left(1 + \alpha_h \frac{t}{\tau_{ps}}\right), \tag{21}$$

and the two coefficients α_H and α_h may be interpreted as two "orthotropization rates." In addition, it is assumed that $C_{vv}(t)$ remains constant in order to limit the number of adjustable parameters:

$$C_{vv}(t) = C_{vv}^{iso}, \quad \forall t \in [0; \tau_{ps}]. \tag{22}$$

The isotropic components are merely calculated by inverting the compliance matrix, and this leads to the following well-known expressions:

$$C_{Hv}^{iso} = C_{hv}^{iso} = \frac{\nu^{iso} E^{iso}}{(1 + \nu^{iso})(1 - 2\nu^{iso})}, \tag{23}$$

$$C_{vv}^{iso} = \frac{(1 - \nu^{iso}) E^{iso}}{(1 + \nu^{iso})(1 - 2\nu^{iso})}. \tag{24}$$

with E^{iso} and ν^{iso} the isotropic drained Young modulus and isotropic drained Poisson ratio, respectively. Since oedometric conditions are considered, equation (16) may be rewritten:

$$\sigma_H(t,z) = \left[\int_0^t C_{Hv}(\tau) : \partial_\tau \epsilon_v(\tau, z)\, \mathrm{d}\tau\right] - b\,\pi_f(t,z) + \sigma_H^{inst}(t,z), \tag{25}$$

$$\sigma_h(t,z) = \left[\int_0^t C_{hv}(\tau) : \partial_\tau \epsilon_v(\tau, z)\, d\tau\right] - b\,\pi_f(t,z) + \sigma_h^{inst}(t,z). \tag{26}$$

If we introduce the two coefficients,

$$K_H^{inst}(t) = \frac{C_{Hv}(t)}{C_{vv}(t)}, \qquad K_h^{inst}(t) = \frac{C_{hv}(t)}{C_{vv}(t)}, \tag{27}$$

and if we assume that the instantaneous stress response due to the time-dependency of elastic properties is given by

$$\sigma_H^{inst}(t,z) = K_H^{inst}(t)\sigma_v(t,z), \tag{28}$$

$$\sigma_h^{inst}(t,z) = K_h^{inst}(t)\sigma_v(t,z), \tag{29}$$

the horizontal total stress finally may be rewritten:

$$\sigma_H(t,z) = \left[\int_0^t C_{Hv}(\tau) : \partial_\tau \epsilon_v(\tau, z)\, \mathrm{d}\tau\right] - b\,\pi_f(t,z) + K_H^{inst}(t)\sigma_v(t,z), \tag{30}$$

$$\sigma_h(t,z) = \left[\int_0^t C_{hv}(\tau) : \partial_\tau \epsilon_v(\tau, z)\, \mathrm{d}\tau\right] - b\,\pi_f(t,z) + K_h^{inst}(t)\sigma_v(t,z). \tag{31}$$

At this stage, we notice that these horizontal stress components are compatible with the mechanical equilibrium (12) since (i) they do not depend on the horizontal space variables x and y and (ii) gravity is vertical.

Let us outline that the various coefficients, which characterize the model, are to be computed so as to fit best the present-day observed stress field, which is—in addition to the pore pressure profile—the only constraining set of data for this problem.

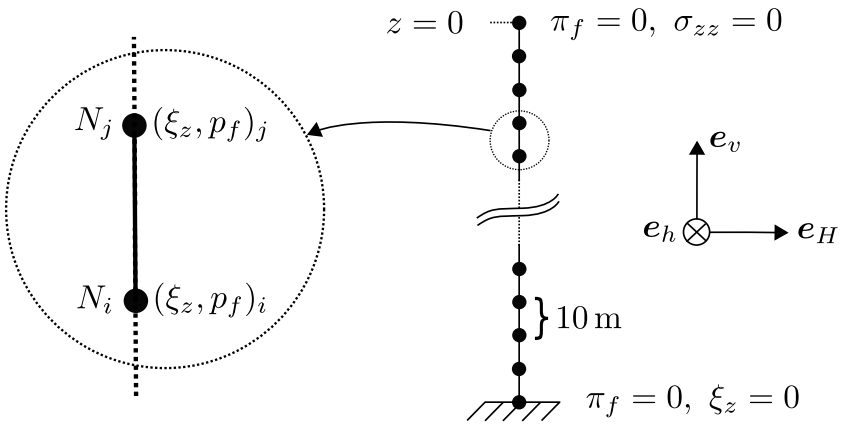

Figure 4. Mesh, boundary conditions, and finite elements used for the proposed one-dimensional hydromechanical viscoelastic model. The finite element pictured as an example joins node N_i to node N_j, each node having 2 degrees of freedom.

3.3. The Initial State

The initial state of stress ($t = 0$) is assumed to be such that $\sigma_h = \sigma_H$ in all geological layers and consistent with equation (18). This stress field coincides with the well-known solution for a semi-infinite body loaded by gravity only under oedometric conditions:

$$\boldsymbol{\sigma}(t=0,z) = \boldsymbol{\sigma}^{\text{inst}}(t=0,z) = \begin{pmatrix} K^{\text{iso}} r_0 g z & 0 & 0 \\ 0 & K^{\text{iso}} r_0 g z & 0 \\ 0 & 0 & r_0 g z \end{pmatrix} \tag{32}$$

with

$$K^{\text{iso}} = \frac{\nu^{\text{iso}}}{1-\nu^{\text{iso}}}. \tag{33}$$

Note that this stress field is compatible with equations (30) and (31) at $t = 0$ (for which we have $\epsilon_v = 0$ and $\pi_f = 0$). In addition, we assume that the initial pressure is hydrostatic:

$$p_f^0(t=0,z) = p_{\text{atm}} - \rho_f g z, \quad z < 0, \tag{34}$$

$p_{\text{atm}} = 10^5$ Pa is the atmospheric pressure.

3.4. Numerical Aspects

The validation of the previous equations is made by comparing experimental data to outputs of a one-dimensional finite elements model supplemented by some postprocessing calculations. Concerning experimental data, vertical profiles of horizontal over vertical stress components ratios are considered, as well as a vertical profile of the fluid overpressure. The modeled counterparts of the latter are obtained as follows. At first, the vertical stress $\sigma_v(t,z)$, the volume strain $\epsilon_v(t,z)$, and the fluid overpressure $\pi_f(t,z)$ are calculated by a one-dimensional finite element model in the vertical space direction. For that purpose, one-dimensional finite elements have been implemented in the French finite element software *Code_Aster* (EDF-R&D, 2016). These elements are two nodes segments, each node having 2 degrees of freedom (the vertical displacement ξ_z and the fluid pressure p_f). The vectorial nonlinear equation giving the nodal increments of generalized displacements (ξ_z, p_f) between t and $t + \Delta t$ is obtained from an Euler-implicit scheme and is solved by using the Newton-Raphson algorithm. During the simulation, the water overpressure vanishes at the top and at the bottom of the mesh ($\pi_f = 0$). For the mechanical boundary conditions, the upper node ($z = 0$) lays on a surface which is stress free, while the bottom node supports no vertical displacement (see Figure 4). All finite elements are 10 m in height.

Once the finite element model is completed, the horizontal stress components $\sigma_H(t,z)$ and $\sigma_h(t,z)$ can be calculated using equations (30) and (31). Finally, the value of the ratios between, respectively, the maximum

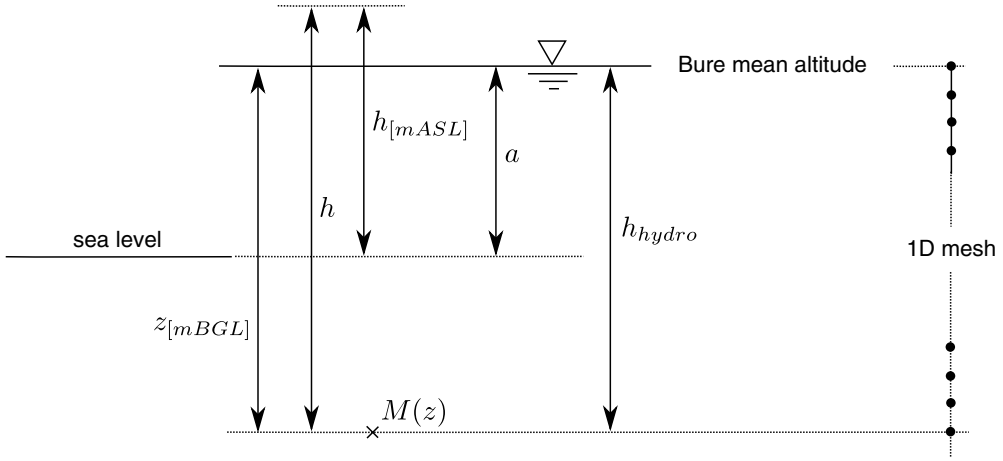

Figure 5. Link between h (head) and $h_{[masl]}$ (head in meters above sea level) for a given point $M(z)$.

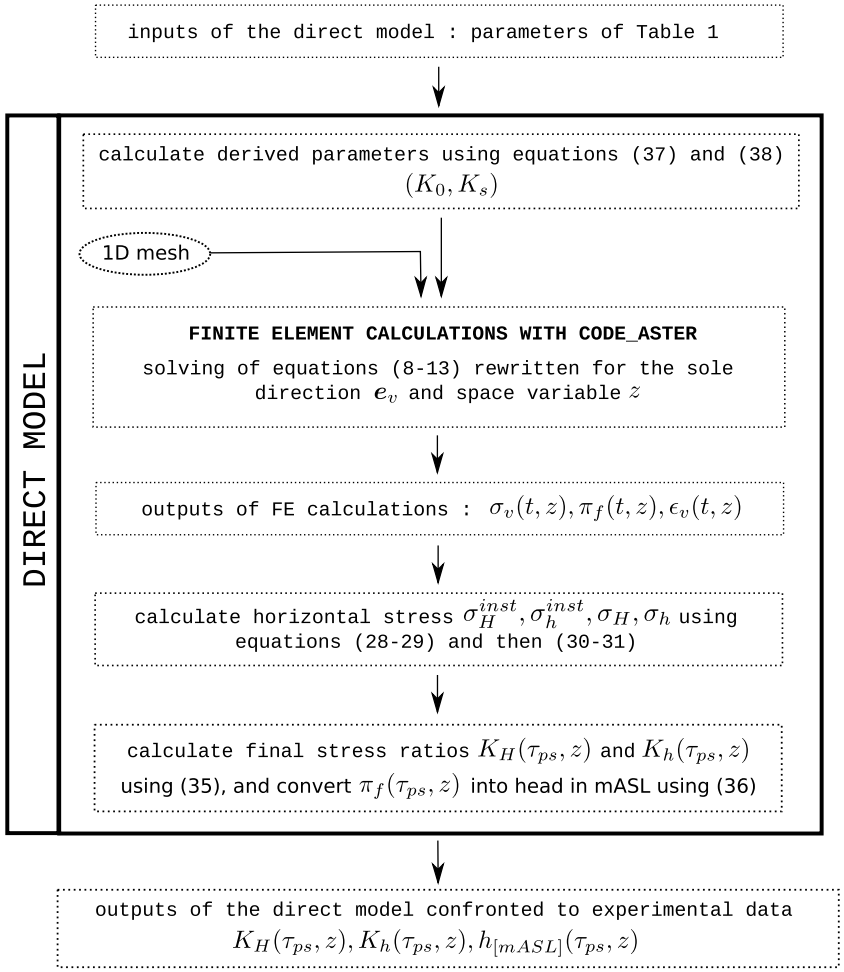

Figure 6. Summary of the numerical procedure, called "direct model," used to calculate $K_H(\tau_{ps}, z)$, $K_h(\tau_{ps}, z)$ and $h_{[masl]}(\tau_{ps}, z)$.

Table 1
Parameters Taken as Inputs of the Model

Name	Description
E^{iso}	isotropic drained Young modulus
ν^{iso}	isotropic drained Poisson's ratio
α_H	anisotropy in the x direction (see equations (20) and (21)
α_h	anisotropy in the y direction
r_0	initial homogenized density
ϕ_0	initial porosity
b	Biot's coefficient
β	pressure solution rate
K^{int}	intrinsic permeability
ρ_f	fluid density
μ_f	fluid dynamic viscosity
τ_{ps}	time constant for pressure solution effects

and the minimum horizontal principal stress components and the vertical stress component at $t=\tau_{ps}$ is calculated:

$$K_H(\tau_{ps},z)=\frac{\sigma_H(\tau_{ps},z)}{\sigma_v(\tau_{ps},z)},\quad K_h(\tau_{ps},z)=\frac{\sigma_h(\tau_{ps},z)}{\sigma_v(\tau_{ps},z)}. \tag{35}$$

For the fluid head profile, the overpressure $\pi_f(\tau_{ps},z)$ is converted into masl (meters above sea level) in order to be compared with data of Delay et al. (2007). The conversion is made via the equation:

$$h_{[masl]}=h-h_{hydro}+a=\frac{\pi_f}{\rho_f g}+a \tag{36}$$

in which $a = 305$ m is the mean altitude of Bure, h the fluid head, and h_{hydro} its hydrostatic counterpart. Figure 5 pictures the different origins used to calculate $h_{[masl]}$. Let us note that, in our model, the medium has been considered as being saturated up to $z = 0$. This is justified by the fact that the mean groundwater depth at Bure is negligible as compared to the minimum depth for which experimental data are available.

For the sake of clarity, the entire procedure called "direct model" is summarized in Figure 6. In order to avoid boundary effects at the bottom side, the thickness of Dogger corresponds to the real value increased by 1,000 m. Consequently, the mesh of the Dogger limestone is 1,227 m thick but only a thickness of 227 m is considered for the postprocessing, that is, for the computation of stress and pressure profiles.

3.5. Model Parameters and Back Analysis

The parameters taken as inputs for the model are listed in Table 1. They are used for evaluating the following secondary parameters necessary for solving the governing equations numerically:

1. K_0: bulk modulus of the drained porous media given by:

$$K_0=\frac{E^{iso}}{3\,(1-2\,\nu^{iso})}. \tag{37}$$

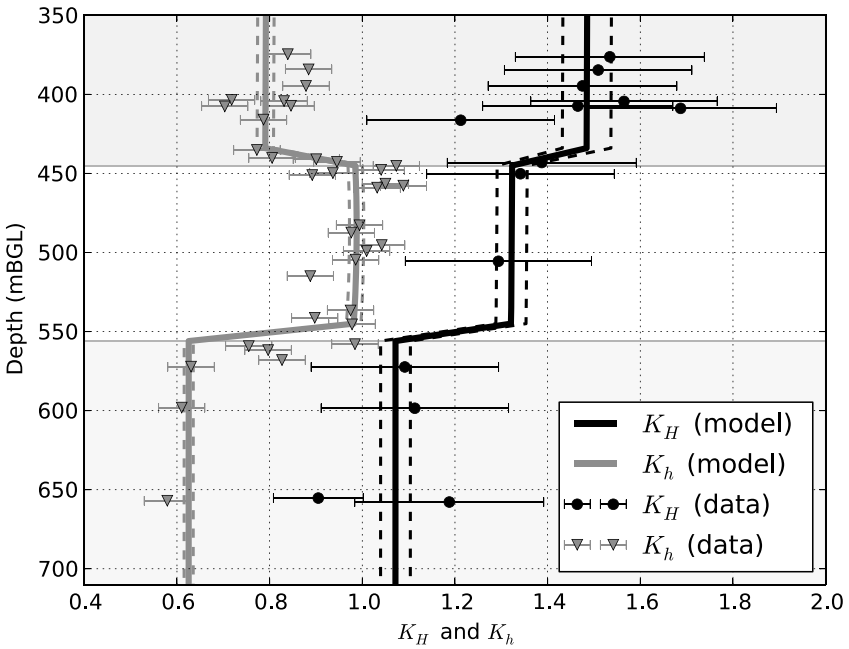

Figure 7. Comparison between model and experimental data (horizontal to vertical stress ratios K_h and K_H). The background gray zones indicate the geological layers. Dashed lines correspond to results obtained by varying α_H and α_h by ±5%.

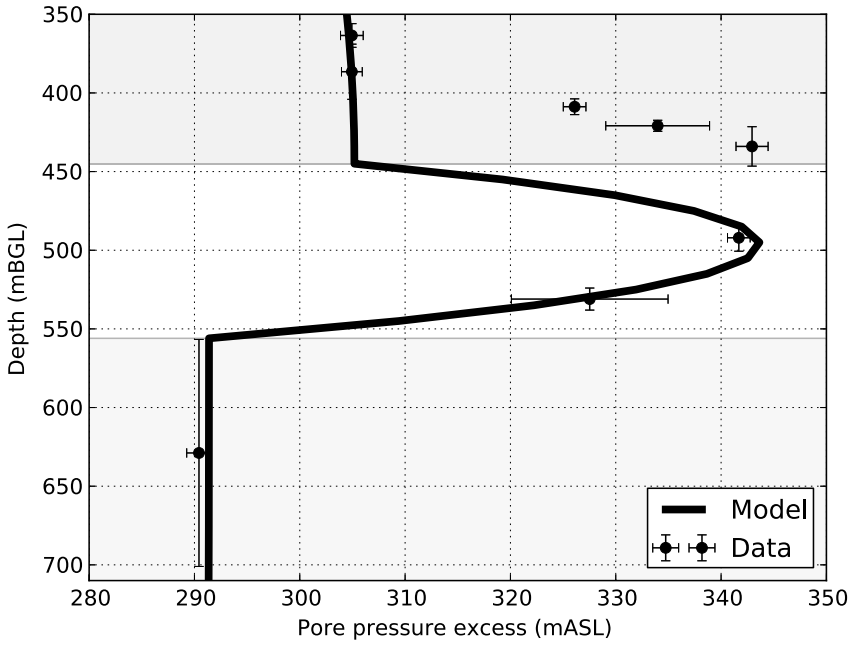

Figure 8. Comparison between model and experimental data of Delay et al. (2007) (overpressure π_f converted in masl). The background gray zones indicate the geological layers.

This coefficient is assumed to remain constant during the numerical simulation, even though the elastic isotropic properties evolve toward anisotropic properties.

2. K_s: bulk modulus of solid grains:

$$K_s = \frac{K_0}{1-b}. \tag{38}$$

Hereafter, the different geological layers are identified by the superscript: "oxf," "arg," and "dog."

The back analysis has been carried out with the Levenberg-Marquardt algorithm (least squares optimization) that has been implemented in the PEST software (Doherty, 2005). Among all input parameters, the following have been estimated: (1) α_H^{oxf}, α_H^{arg}, and α_H^{dog} (and their equivalent for the h direction): orthotropization rates

Table 2
Values of Parameters

Rheological parameters	Oxfordian	Argilite	Dogger	Fluid	Other
E^{iso} (GPa)	1.0	1.0	1.0	—	—
ν^{iso}	0.30	0.40	0.30	—	—
α_H	*2.45*	*0.98*	*1.50*	—	—
α_h	*0.83*	*0.47*	*0.46*	—	—
r_0 (kg m^{-3})	2,450	2,450	2,450	—	—
ϕ_0	0.10	0.01	0.10	—	—
b	0.90	0.90	0.90	—	—
β (g m^{-3} a^{-1})	*49.3*	*0.111*	*0.807*	—	—
K^{int} (m^2)	10^{-15}	10^{-20}	10^{-15}	—	—
ρ_f (kg m^{-3})	—	—	—	1,000	—
μ_f (Pa s)	—	—	—	10^{-3}	—
τ_{ps} (a)	—	—	—	—	*3,487*

Note. The italicized values have been obtained by back analysis.

in both horizontal directions, for the three geological layers under consideration; (2) β^{oxf}, β^{arg}, β^{dog}: pressure solution rates; and (3) τ_{ps} : pressure solution characteristic time, taken as the total duration of the simulation.

Results of the best fit are given in Figures 7 and 8. They outline a good agreement between numerical model and experimental data. Values for the various parameters associated with this best fit are listed in Table 2. In order to investigate the influence of small variations in α_H and α_h values on the solution, we have considered $\pm$5% variations for these parameters. Results are illustrated by the dashed lines on Figure 7. They indicate that uncertainties on the stress measurements are too large to provide a strong constraint on the best solution.

In Figure 8 we note that the model yields results for the pore pressure that are smaller than observed data in the 400–450 m depth range. This is because, in the absence of direct measurements, we have assumed that permeability and elastic coefficients are both only related to the geological definition of the various layers. This small discrepancy could easily be corrected numerically by assuming that the permeability in the lower part of the Oxfordian limestone is much lower than that in its upper part of this layer because of some soft clay particles in the pore space. Only direct in situ permeability measurements would help resolve more forcefully this issue.

4. Discussion and Perspectives

4.1. What time Constant for Pressure-Solution Effects?

As pointed out earlier, the τ_{ps} parameter is a time constant characteristic of pressure solution effects. Yasuhara and Elsworth (2004) showed that the rate of fracture closure linked to pressure solution effects is strongly temperature dependent. It is associated to both dissolution rates and precipitation rates, which are strongly material dependent. In the present investigation, no attention has been given to the physical factors that control its value. Despite the fact that τ_{ps} has been estimated by the least squares method, its value is not physically significant in our model. It strongly depends on the values of β and of permeability.

When the fluid is at rest, as pressure solution develops, the ion concentration in the fluid close to the fracture asperities reaches progressively some equilibrium. Hence, the correlated volumetric deformation rate decreases with time till it vanishes completely. The model proposed here above is only phenomenological, and we made no attempt at modeling the nanoscale phenomena associated with pressure solution. We only conclude that, in a closed system, τ_{ps} is finite so that the period during which pressure solution occurs after a tectonic phase remains finite.

4.2. Dependence of the Present-Day Stress Field on Climatic Variations

When some fluid motion occurs, pressure solution may become a continuing process since the ions content in the liquid never gets at equilibrium with the stressed solid asperities. Interestingly, detailed modeling of the long-term hydrodynamic response induced by past climatic forcing has been conducted by Jost et al. (2007) for the ground water system encountered in the Paris Basin sedimentary formations. Particular attention has been given to the locality of the Underground Research Laboratory at Bure, where the stress determination has been conducted. They found that because of the development of permafrost during glaciation periods, water infiltration was stopped over large area and this resulted in decline in water pressure at certain depths. Jost et al.'s (2007) simulations outline spatial pressure variations with time characteristics that are those of the past climatic variations, that is, variations that scale in tens to hundreds of thousand years. They imply transient local pressure gradients with similar time characteristics. These changing local pressure gradients generate some local fluid motions that affect the ions densities in the water close to zones of stress concentrations and therefore affect pressure solution effects. According to Jost et al.'s (2007) work, climatic variations are clearly felt down to the argillite and therefore within the overlying Oxfordian limestones. Hence, in this limestone layers, development of pressure solution effects depend on climatic variations and therefore so does the stress field in this formation, and so does that in the various overlying limestones.

4.3. Origin of the Overpressure Observed in the Callovo-Oxfordian Argillite

In our model, the effect of pressure solution is twofold: first, it affects the large-scale elastic characteristics of geomaterials and second, it generates perturbations in the pore pressure of saturated geomaterials. The dissipation of such pore pressure perturbations depends in turn on the volumetric strain rate associated with pressure solution effects (parameter β in equation (8) and on the permeability of the geomaterials of concern. For the data inversion conducted with our model, the overpressure observed in the argillite requires that the coefficient β for the argillite be about 500 times smaller than that associated with the overlying limestone.

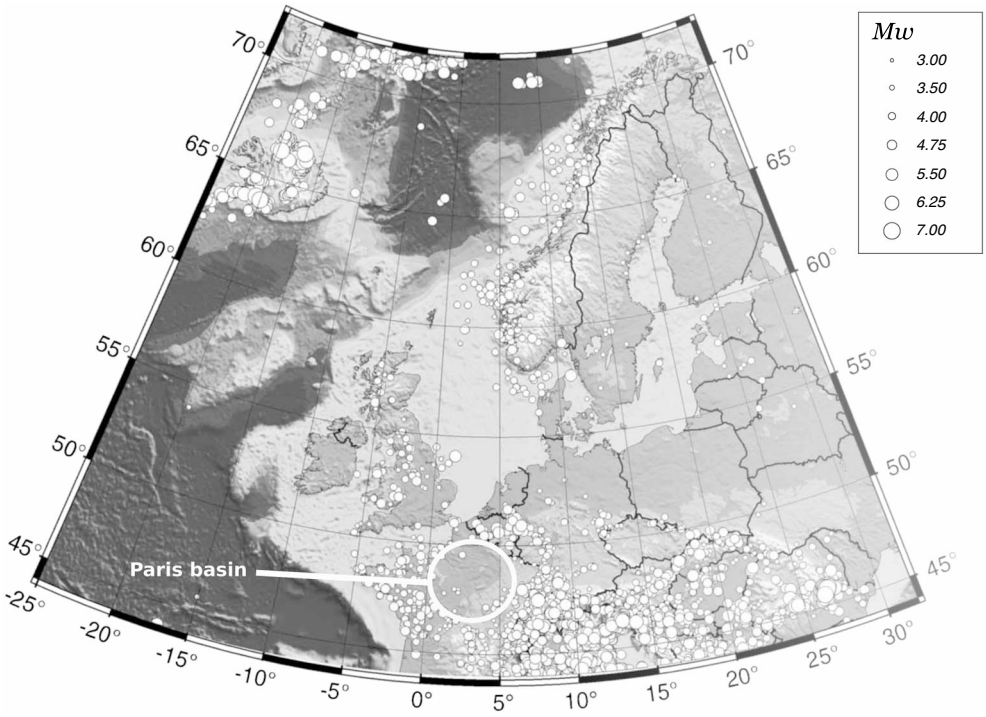

Figure 9. Map of northwestern Europe seismicity, slightly adapted from Grünthal and Wahlström (2003) in order to point out the Paris sedimentary basin.

This is quite consistent with the observation that only very few preexisting vertical fractures have been observed in the argillite (André et al., 2006). However, no direct analysis of pressure solution has been conducted so that we cannot conclude, at this stage, that indeed, the overpressure observed in the argillite is only linked to pressure solution effects within these very few preexisting vertical fractures.

In fact, another possible model would take into account the spatial variability of the density of vertical fractures in all the geomaterials. This would require a true 3-D model that might account for the fact that the fracture density follows more or less a periodic distribution in the horizontal directions. With such a model, periodic lateral variations in elastic parameters would be introduced. This would result in interactions between the various layers depending on the boundary conditions imposed at the various layers interfaces. This feature has not been explored here in order to keep the model as simple as possible. However, it should be mentioned that local rotations of the principal stress directions have been observed close to the interface between the Oxfordian limestone and the underlying Callovo-Oxfordian argillite. This clearly demonstrates the existence of local slippage between these two layers and therefore the existence of lateral variations in the mechanical characteristics of the Oxfordian limestone. These horizontal variations generate some nonuniform shear stress at the horizontal interface between the Oxfordian limestone and the argillite layer. An important question that remains to be answered is to evaluate the pore pressure effect, in the argillite, associated with the transfer of horizontal strain between the Oxfordian limestone and the argillite.

4.4. Stress Profiles and the Long-Term Rheology of Geomaterials

The one-dimensional model, which has been presented, implies that the vertical variations of the stress field in the Paris sedimentary basin do not depend on the present-day stresses at greater depths. Indeed, it has been argued that it depends on gravity effects on geomaterials, the long-term rheological characteristics of which are time dependent and become progressively orthotropic. In this model, the maximum horizontal principal stress component may become larger than the vertical component, depending on the elastic coefficients.

But other mechanisms have been proposed for explaining the common observation that, in many area where crystalline rocks are encountered, the average of both principal horizontal stress components at zero depth is not null and may reach values as high as 40.5 MPa (Engelder & Sbar, 1984). Interestingly, for many of these sites, it was also observed that the strike of microcracks observed in these rocks was parallel to the maximum

horizontal principal stress direction. This resulted in anisotropic dynamic elastic rock properties, as outlined by *P* wave velocity measurements conducted in the field.

Hence, we may conclude that the orthotropic hypothesis is valid for a large variety of geomaterials and should be taken into account when analyzing regional stress fields. Clearly, these long-term elastic coefficients differ significantly from the dynamic ones and conducting stress measurements in various directions would help identifying the complete "long-term" compliance matrix.

4.5. Deep Fluid Motion and Microseismicity

The map of Europe seismicity (Grünthal & Wahlström, 2003) shows that some continuous seismic activity is observed in the crystalline and metamorphic massifs that surround the Paris Basin, when none is observed in the Paris Basin basement (Figure 9). But some of these massifs are at similar distances from plate boundaries as is the Paris Basin. A similar observation may be made for the northern German sedimentary basin. This raises difficulty to link observed seismicity to plate boundary conditions as outlined by Calais et al. (2016).

We note that in the Paris Basin, the Callovo-Oxfordian argillite prevents any downward fluid flow between ground surface and the basement rock, when no such impervious barrier exists in the surrounding massifs where some microseismicity is observed. Similarly, in the north German sedimentary basin, the Zechstein salt layer prevents any surface perturbation of fluid flow from reaching the formations below the evaporitic layers. It may be proposed that chemical interactions associated with deep fluid motions in crystalline and metamorphic massifs affect their anisotropic viscoelastic characteristics. This results in time variations of the relative principal stress magnitudes associated with gravity loading only and may lead to episodic local instabilities. Hence, microseismicity would simply be generated by the effect of gravity alone on an anisotropic material, the anisotropic characteristics of which are linked to deep fluid motions. We propose that such a mechanism may be considered as part of the new paradigm introduced by Calais et al. (2016) for their analysis of intraplate seismicity.

5. Conclusions

Jost et al. (2007) have shown that, at Bure, climatic variations generate fluid motions within the Oxfordian limestone that overlay the Callovo-Oxfordian argillite. These in turn induce temporal variations in the pressure solution that develops within the natural fracture system that affects this limestone. Consequently, the limestone gets progressively orthotropic so that, through the effect of gravity only, differential horizontal stresses are generated.

But pressure solution generates also a decrease in volumetric strain that generates an overpressure. For materials with very low permeability, like the Callovo-Oxfordian argillite, this generates overpressure transients. Another possible mechanism at the origin of the observed argillite overpressure, which has not been explored here, is the shear coupling that may develop between the various layers because of this change in material properties with time.

This analysis has shown that because of pressure solution and climatic variations, the mechanical characteristics of some sedimentary materials vary with time and become anisotropic. These continuously changing material properties induce both regional stress variations and pore pressure transients in the most impervious layers, with time constants that scale in thousands to ten thousands of years.

More generally, we conclude that the stress field in sedimentary formations encountered in intraplate domains may not represent the deeper stress field encountered in the basement rock. In domains where tectonics implies deformation rates slower than those which control the viscoelastic behavior of the sedimentary layers, stress measurements or observation of present-day deformations in sediments cannot be directly transposed to greater depths.

Finally, we infer from the location of microseismic activity in northwestern Europe that such a fluid-solid chemical interaction may play an important role in intraplate stress fields.

Acknowledgments
Data used in this work can be obtained from cited references. FORTRAN subroutines and header files used to overload *Code_Aster* can be downloaded from http://vincentmagnenet.free.fr/JGR2017/JGR2017_Magnenet_et_al_Fortran.zip. The authors are grateful to E. Calais, D. Elsworth, S. Medvedev, and J. Virieux for their helpful suggestions at various stages of this work.

References

André, G., Proudhon, B., Rebours, H., & Willeveau, Y. (2006). Paramètres contrôlant la distribution de la fracturation: exemple dans une série marno-calcaire du Jurassique supérieur (Est du bassin de Paris). *Comptes Rendus Geoscience*, *338*, 931–941.

Calais, E., Camelbeeck, T., Stein, S., Liu, M., & Craig, T. J. (2016). A new paradigm for large earthquakes in stable continental plate interiors. *Geophysical Research Letters*, *10*, 621–637. https://doi.org/10.1002/2016GL070815

Cara, M., Cansi, Y., Sclupp, A., Arroucau, P., & Béthoux, N. (2015). SI-Hex: A new catalogue of instrumental seismicity for metropolitan France. *Bulletin de la Societe Geologique de France*, *186*, 3–19.
Cornet, F. H., & Roeckel, T. (2012). Vertical stress profiles and the significance of stress decoupling. *Tectonophysics*, *581*, 193–205.
Coussy, O. (2004). *Poromechanics*. Chichester, United Kingdom: John Wiley & Sons.
de Marsily, G. (1986). *Quantitative Hydrogeology*. Orlando, FL: Acadamic Press.
Delay, J., Distinguin, M., & Dewonck, S. (2007). Characterization of a clay-rich rock through development and installation of specific hydrogeological and diffusion test equipment in deep boreholes. *Physics and Chemistry of the Earth*, *32*, 393–407.
Doherty, J. (2005). PEST version 9.0 users guide. Watermark Numerical Computations. Retrieved from http://www.pesthomepage.org
EDF-R&D (2016). Code_Aster open source—General FEA software. Retrieved from www.code-aster.org
Engelder, T., & Sbar, M. L. (1984). Near-surface in-situ stress: Introduction. *Journal of Geophysical Research*, *89*, 9321–9322.
Gonçalves, J., Violette, S., & Wendling, J. (2004). Analytical and numerical solutions for alternative overpressuring processes: Application to the Callovo-Oxfordian sedimentary sequence in the Paris Basin, France. *Journal of Geophysical Research*, *109*, B02110. https://doi.org/10.1029/2002JB002278
Gonçalves, J., Violette, S., Guillocheau, F., Robin, C., Pagel, M., Bruel, D., … Ledoux, E. (2004). Contribution of a three-dimensional regional scale basin model to the study of the past fluid flow evolution and the present hydrology of the Paris Basin, France. *Basin Research*, *16*, 569–586.
Gratier, J. (1993). Experimental pressure solution of halite by an indenter technique. *Geophysical Research Letters*, *20*, 1647–1650. https://doi.org/10.1029/93GL01398
Gratier, J. P., & Guiguet, R. (1986). Experimental pressure solution-deposition on quartz grains: The crucial effect of the nature of fluid. *Journal of Structural Geology*, *8*, 845–856.
Grünthal, G., & Wahlström, R. (2003). An M_w based earthquake catalogue for central, northern and northwestern Europe using a hierarchy of magnitude conversions. *Journal of Seismology*, *7*, 507–531.
Gundersen, E., Renard, F., Dysthe, D. K., Bjørlykke, K., & Jamtveit, B. (2002). Coupling between pressure solution creep and diffusive mass transport in porous rocks. *Journal of Geophysical Research*, *107*(B11), 2317. https://doi.org/10.1029/2001JB000287
Gunzburger, Y., & Cornet, F. H. (2007). Rheological characterization of a sedimentary formation from a stress profile inversion. *Geophysical Journal International*, *168*, 402–418.
Gunzburger, Y., & Magnenet, V. (2014). Stress inversion and basement-cover stress transmission across weak layers in the Paris Basin, France. *Tectonophysics*, *617*, 44–57.
Holl, J. E., & Anastasio, D. J. (1995). Cleavage development within a foreland fold and thrust belt, southern Pyrénées, Spain. *Journal of Structural Geology*, *17*, 357–369.
Jost, A., Violette, S., Gonçalves, J., Ledoux, E., Guyomard, Y., Guillocheau, F., … Suc, J. P. (2007). Long-term hydrodynamic response induced by past climatic and geomorphologic forcing: The case of the Paris Basin, France. *Physics and Chemistry of the Earth*, *32*, 368–378.
Laubsher, H. P. (1975). Viscous components in Jura folding. *Tectonophysics*, *27*, 239–254.
Lefeuvre, F., Nicoletis, L., Ansel, V., & Cliet, C. (1992). Detection and measure of birefringence from vertical seismic data: Theory and applications. *Geophysics*, *57*, 1463–1481.
Neuzil, C. E. (1995). Abnormal pressures as hydrodynamic phenomena. *American Journal of Science*, *295*, 742–786.
Nocquet, J. M. (2012). Present-day kinematics of the Mediterranean: A comprehensive overview of GPS results. *Tectonophysics*, *579*, 220–242.
Schmalholz, S. M., Medvedev, S., Lechmann, S. M., & Podlachikov, Y. (2014). Relationship between tectonic overprerssure, deviatoric stress, driving force, isostasy and gravitational potential energy. *Geophysical Journal International*, *197*, 680–696.
Schneider, F., Potdevin, J. L., Wolf, S., & Faille, I. (1996). Mechanical and chemical compaction model for sedimentary basin simulators. *Tectonophysics*, *263*, 307–317.
Talbot, C. J. (1999). Can field data constrain rock viscosities? *Journal of Structural Geology*, *21*, 949–957.
Wileveau, Y., Cornet, F. H., Desroches, J., & Blumling, P. (2007). Complete in situ stress determination in an argillite sedimentary formation. *Physics and Chemistry of the Earth*, *32*, 866–878.
Yasuhara, H., & Elsworth, D. (2004). Evolution of permeability in a natural fracture: Significant role of pressure solution. *Journal of Geophysical Research*, *109*, B03204. https://doi.org/10.1029/2003JB002663